Nanoscale

Accepted Manuscript

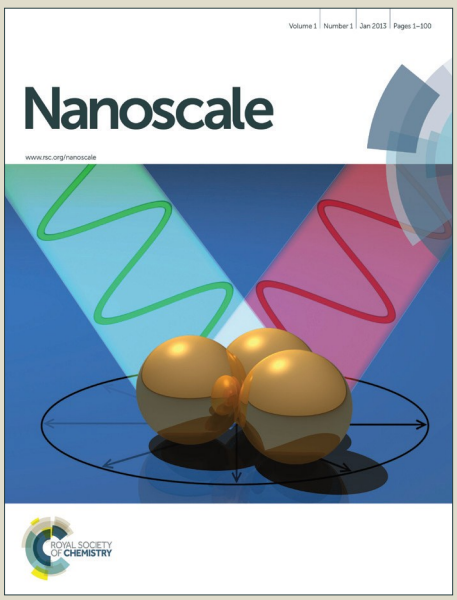

ROYAL SOCIETY OF CHEMISTRY

www.rsc.org/nanoscale

Journal Name

RSCPublishing

ARTICLE

Particulates Vs fibers: Dimension featured magnetic and visible light driven photocatalytic properties of Sc modified multiferroic bismuth ferrite nanostructures

Cite this: DOI: 10.1039/x0xx00000x

Received ooth January 2012,
Accepted ooth January 2012

DOI: 10.1039/x0xx00000x

www.rsc.org/

M. Sakar,[a] S. Balakumar,[a,*] P. Saravanan,[b] S. Bharathkumar[a]

We report the magnetic and visible light driven photocatalytic properties of scandium (Sc) substituted bismuth ferrite (BSFO) particulates and fibers nanostructures. The increasing concentration of Sc was found to reduce the crystallite, particle size and band gap energy of BSFO nanostructures, which was evident from X-ray diffraction, field emission scanning electron microscopy and UV-Visible diffuse reflectance spectroscopy analysis respectively. The temperature dependent magnetic studies carried out by using SQUID magnetometer suggested that the origin of magnetic properties in pure BFO system could be the emergence of antiferromagnetic-core/ferromagnetic-shell like structure, whereas the modified spin canted structures in the case of BSFO nanostructures. The observed photocatalytic efficiency was attributed to the enhanced band bending process and recombination resistance in these BSFO nanostructures. For a comparative study, the photocatalytic activities of some selected compositions were also investigated under the simulated solar light along with the natural solar light.

1. Introduction

The coexistence of two or more primary ferroic orders in a single phase material is known as multiferroics which has drawn significant attention in many fields, to name a few, magnetic storage, spintronics, transducers and four stage memory device applications.[1,2] In the perspective of fundamental physics, the embodiment of magnetic and ferroelectric properties in a single phase material is an atypical phenomenon since the spin of the electrons governs the magnetic properties and the charge of electrons or ions is responsible for electrical polarization in materials.[3] In other words, the typical magnetic materials are often metallic and ferroelectric materials are likely insulators and therefore it is relatively hard to achieve such blend of phenomena holding up both properties in a single phase state of a material. Nevertheless, this has been phenomenally manifested in the multiferroic materials wherein these two properties have emerged via controlling the population of electrons in '*d*' shell.[4] For instance, the filled '*d*' shell leads to ferroelectricity while the empty '*d*' shell causes magnetism in the multiferroic materials.[5-8]

Towards understanding the phenomena of multiferroics, bismuth ferrite ($BiFeO_3$-BFO), is realized to be a prototypical multiferroic material that shows spontaneous ferroelectricity and antiferromagnetism at room temperature.[9] BFO is a perovskite structured material belonging to rhombohedral crystal system with *R*3*c* space group and possess very high anti-ferromagnetic Neel (T_N) and ferroelectric Curie (*Tc*) temperatures around 643 K and 1100 K, respectively.[10] The ferroelectric property in BFO emerges due to the off-centred distortion of Fe ions, originates by $6s^2$ lone pair electrons of Bi^{3+} ions in its non-centrosymmetric rhombohedral structure. Similarly, the magnetic property appears due to the partially filled 3*d* orbital of Fe^{3+} ions that lead to *G*-type canted antiferromagnetic order with an incommensurated spin structure with the wavelength period of 62 nm.[11, 12] In addition to its multiferroic features, in recent years, BFO is also being extensively investigated for its photo-driven properties towards photovoltaic (PV) and photocatalytic (PC) applications owing to its optimum band gap energy (~2.2 eV) that capable of driven by the visible light.[13] The PC property of BFO is considered as one of the appealing features that can be potentially used for water-splitting process to produce hydrogen and environment cleaning application via degrading organic dyes, etc.[14] Therefore, customizing materials' property is required for the effective utilization of materials for the intent applications. In this context, the origin of photo-driven property in BFO can be investigated in the perspective of a 'ferroic-

semiconductor', where it is characterized by its inherent inter-coupled magnetic and ferroelectric properties.[15] Enhancing its ferroelectric properties helps BFO by prolonging the charge separation during the depolarization of electric field that significantly reduces the recombination effect in BFO through a process known as band bending phenomenon.[16-18]

In addition to the materials' unique inherent and external modifications-induced properties, their enhanced photocatalytic activity is also dependent upon the structure parameters such as size and dimension of the materials.[19] One dimensional (1D) nanostructures show enhanced physical and chemical properties owing to their fettered and unfettered dimensions where a synergic quantum and bulk effect can be observed in their physical and chemical properties.[20] It is anticipated that the dimension dependent physical properties of materials can be clearly perceived in the case of a comparative study carried out on one-dimensional *vs.* particulate systems. In this context, here we report our results on the magnetic and natural and simulated solar-light driven photocatalytic studies of scandium (Sc) substituted BFO particulate and fiber nanostructures.

The selection of Sc as well as the substitution site is because of the following factors which are revealed through the first-principle density functional theory calculations by Zhen Zhang, et al.[21] They have reported that (i) the substitution of Sc^{3+} ions in 'Bi' site causes very large off-center displacement and gives rise to a stronger ferroelectricity, (ii) Due to small ionic radius (R_{Bi}^{3+} = 1.24 Å, R_{Sc}^{3+} = 0.92 Å) and larger electronegativity difference of Sc-O (2.08) compared to Bi-O (1.42), causes stronger Sc-O hybridization, and (iii) Sc substitution also reduces the band gap energy of BFO owing to the Fe-O-Fe super-transfer mechanism resulting from the overlapping of conduction band (Sc 3*d* states) and valence band (O 2*p* states). Within the scope of our studies, it is expected that the above theoretical results on Sc substituted BFO would be supportive for the experimental characterization of their magnetic and photocatalytic properties. In which, (i) the structural distortion and hybridization would enhance the ferroelectric and magnetic properties, (ii) the ferroelectric enhancement would facilitate the recombination delay, and (iii) reducing band gap energy would induce visible light absorption of BFO, and a consequent enhancement in their photocatalytic properties. Nevertheless, there are hardly experimental reports available on the investigation of Sc substituted BFO nanoparticles and no reports available on Sc substituted BFO nanofibers and their visible light driven photocatalytic properties hitherto.

It could be seen that BFO is recently explored for their photo-driven properties, which has the potential that could be realized to be a next generation photocatalytic material. Compare to the conventional photocatalysts, which are typically semiconductors, BFO as being a multiferroic-semiconductor would open up new possibilities in the field of photocatalysis. Therefore, the novelty of the reported work involves that to study the simultaneous response of BFO during its modification in its dimension such as particulates and fibers, as well as its compositional modifications such as rare earth substitutions. Similarly, towards industrial scale applications, it would be essential to explore their photocatalytic properties under both natural and simulated solar lights. Further, the phenomenon involved in the photocatalytic process of BFO is appealing in terms of its ferroelectric band bending process, which is possibly giving new insights into the positioning of their band edges towards photocatalytic water splitting applications for the hydrogen generation.

2. Experimental

The reagents used for the synthesis were of high-purity bismuth nitrate [$Bi(NO_3)_3 \cdot 6H_2O$] (Puratronic®, 99.999%), iron nitrate [$Fe(NO_3)_3 \cdot 9H_2O$] (Puratronic®, 99.999%), and scandium nitrate [$Sc(NO_3)_3$ $5H_2O$] (REacton®, 99.99%) procured from commercial resources (Alfa Aesar). All the fabrication processes were carried out under ambient conditions.

2.1. Synthesis of $Bi_{1-x}Sc_xFeO_3$ nanoparticulates

The conventional sol-gel method was employed for the synthesis of $Bi_{1-x}Sc_xFeO_3$, (where x = 0.0, 0.05, 0.10, 0.15, 0.20, 0.25) nanoparticulates (NP_S) as reported previously.[22] In a typical procedure for pure BFO particulates, the equivalent grams of 0.1 M bismuth nitrate and iron nitrate precursors were taken in 30 ml of de-ionized water and completely dissolved by adding 2 ml of 70% concentrated nitric acid (HNO_3). To this 0.1 M of citric acid ($C_6H_8O_7$) was added to obtain a homogeneous sol. Then this sol was heated up to ~80 ^{0}C to obtain the gel and dried to powders. The same procedure was repeated by adjusting the amount of bismuth nitrate and adding the appropriate substitution amount of scandium nitrate as per the composition formula to obtain the Sc substituted BFO particulates. Finally, all the synthesized as-prepared powders were annealed at 650 ^{0}C for 3 h to obtain the phase BFO.

2.2. Fabrication of $Bi_{1-x}Sc_xFeO_3$ nanofibers

The nanofibers (NFs) of $Bi_{1-x}Sc_xFeO_3$ (where x = 0, 0.05, 0.1 and 0.15) were fabricated by electrospinning method by slightly modifying the procedure which we previously reported.[23] In the process, for pure BFO fibers, equivalent grams of 0.8 M bismuth nitrate and iron nitrate precursors were taken in 10 ml solution mixture of glacial acetic acid ($C_2H_4O_2$) and de-ionized water to obtain a homogenous sol. To this, 1 g of polyvinyl pyrrolidone (PVP - M.W. 13, 00, 000) was added and stirred for 6 h to get a homogenous final precursor gel like solution for the electrospinning process. Then, this solution was loaded in a stainless steel needled plastic syringe and connected to a high voltage of 15 kV with the solution flow rate of 0.2 ml/h. An aluminium foil spread-fiber collector was kept at a distance of 12 cm from the needle to collect the fibers. The same procedure was repeated by adjusting the amount of bismuth nitrate and adding the appropriate substitution amount of scandium nitrate as per the composition formula of the materials to obtain the Sc substituted BFO nanofibers. Subsequently, the as-electrospun B(Sc)FO/PVP fibers were collected and annealed at 550 ^{0}C for 2 h to obtain the phase BFO.

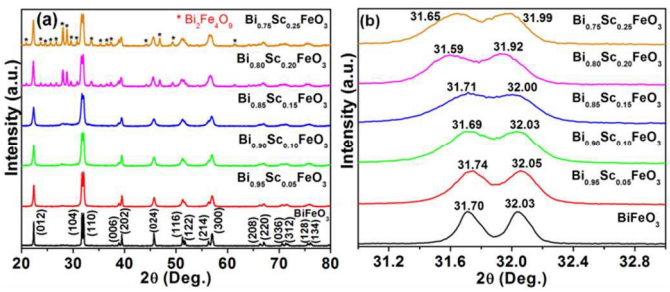

Fig. 1 XRD pattern of (a) $Bi_{1-x}Sc_xFeO_3$ particulate compositions and (b) observed peak shift in the doublet peaks.

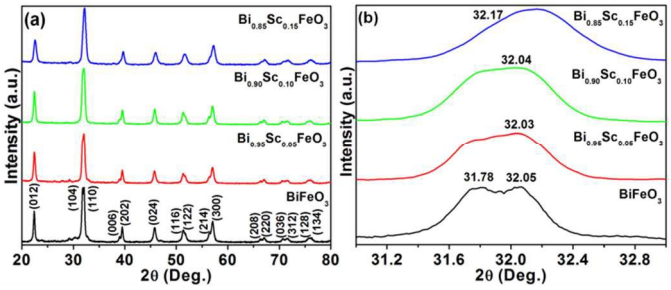

Fig. 2 XRD pattern of (a) $Bi_{1-x}Sc_xFeO_3$ fiber compositions and (b) observed peak shift in the doublet peaks.

2.3. Photocatalytic experiment

The photocatalytic activity of the fabricated pure and Sc substituted BFO particulate and fiber nanostructures were studied under sunlight on the degradation methylene blue (MB) dye. In the experiment, 5 mg of photocatalyst was taken in a 100 ml of MB solution from the stock of 10 mg/L and kept under the irradiation of direct sunlight. The subsequent degradation of MB was recorded in periodical intervals by using UV-Visible absorption spectrometer. Throughout the experiment, the intensity of sunlight was measured for every 30 min, and the average sunlight intensity over the duration of each experiment was also calculated. The intensity of sunlight was measured using LT-Lutron LX-10/A digital Lux meter and the intensity was $1.2 \times 10^5 \pm 100$ lux.

For a comparative study, the photocatalytic activity of the selected samples was also investigated under the simulated solar light source. No filters were used to avoid the UV and IR wavelengths as to nearly mimic the spectrum of natural solar-light. A 500 W arc Xe lamp with an AM 1.5 was used as the simulated solar-light source. The intensity of simulator solar light was found to be ~ 0.9×10^5 lux. The dye-catalyst solution average temperature was found to be around 28 ± 1 °C and 30 ± 1 °C under solar and simulated solar light irradiations respectively.

2.4. Materials characterizations

All the fabricated $Bi_{1-x}Sc_xFeO_3$ particulate and fiber compositions were characterized for their crystal structure and phase analysis by X-ray diffraction technique (XRD-PANalytical Instruments), chemical oxidation state analysis by X-ray photoelectron spectroscopy (XPS-Omicron Nanotechnologies) techniques. The morphology analysis was carried out using the field emission scanning electron microscopy (FESEM-Hitachi HighTech SU6600), and high resolution transmission electron microscopy (HRTEM-Techni G2 S-TWIN, FEI) techniques. Magnetic properties such as field and temperature dependent magnetizations were characterized using the super conducting quantum interference device (SQUID-Quantum Design). Band gap energy was estimated using the UV-Visible diffuse reflectance spectroscopy technique. Further, the optical absorption properties and photocatalytic experiments were carried out using the UV-Visible absorption spectroscope (UV-Vis Abs/DRS-Perkin Elmer).

3. Results and Discussions

3.1. Crystal structure analysis

The powder X-ray diffraction pattern of $Bi_{1-x}Sc_xFeO_3$ (BSFO) particulates (where x=0.0, 0.05, 0.10, 0.15, 0.20, 0.25) and fiber nanostructures (where x=0.0, 0.05, 0.10, 0.15) are shown in Fig. 1(a) and 2(a), respectively. All the diffraction peaks are well indexed to rhombohedral structure (*R*3*c* space group) of $BiFeO_3$ phase (JCPDS Card No. 71-2494). It is evident from the XRD patterns that no additional peaks corresponding to the typical secondary or impurity phases appeared in pure and Sc substituted BFO particulates and fiber systems up to 15% concentration of Sc in the BFO host. However, the secondary phase $Bi_2Fe_4O_9$ was formed along with BFO phase when the concentration of Sc was increased to 20% and 25% in the particulate system. It is noteworthy that such secondary phase appeared in the case of sol-gel synthesized thin films[24] and sonochemically[25] synthesized nanoparticles of Sc-BFO even at 5% and 10% Sc substitution in BFO host, respectively. Accordingly, we propose that our synthesis method is relatively effective for the substitution of Sc at higher concentrations.

On the other hand, we found difficulties during the fabrication of Sc substituted BFO fibers at higher concentrations ($x \geq 0.2$), where the as-spun fiber formation was itself too meagre and sticky, even though the parameters such as solution viscosity, applied voltage were varied systematically. It is known that the electrospinning solution is basically ionic and its interaction with applied voltage is very basis for the fiber formation. Therefore, we believed that the introduction of rare earth ions beyond certain concentrations causes some imbalance in the ionic state/charge of the solution as a whole and resists the fiber formation. We realized that still rigorous studies are required to optimize this current process of the fabrication of Sc substituted BFO nanofibers at higher concentrations.

The average crystallite size of the synthesized pure BFO and BSFO particulates and fibers was calculated by using the Scherrer's formula ($t = 0.9\,\lambda / \beta \cos\theta$), corresponding to (012), (104) and (110) planes. The lattice constants, crystallite size

and strain of these nanostructures were also calculated during the data collection by using the inbuilt software that supplied along with the XRD system (PANalytical-X'pert High-Score) and the obtained values are given in Table 1.

Table 1. Crystal structure parameters of the fabricated compositions.

System	Compositions	$a = b$	c	V	η	t
Particulates	$BiFeO_3$	5.579	13.872	431.77	0.131	51
	$Bi_{0.95}Sc_{0.05}FeO_3$	5.582	13.854	431.67	0.221	37
	$Bi_{0.90}Sc_{0.10}FeO_3$	5.586	13.850	432.17	0.281	29
	$Bi_{0.85}Sc_{0.15}FeO_3$	5.591	13.846	432.82	0.345	24
	$Bi_{0.80}Sc_{0.20}FeO_3$	5.602	13.906	436.40	0.284	29
	$Bi_{0.75}Sc_{0.25}FeO_3$	5.598	13.896	435.47	0.279	30
Fibers	$BiFeO_3$	5.582	13.808	430.24	0.304	27
	$Bi_{0.95}Sc_{0.05}FeO_3$	5.596	13.715	429.48	0.469	23
	$Bi_{0.90}Sc_{0.10}FeO_3$	5.594	13.724	429.46	0.482	21
	$Bi_{0.85}Sc_{0.15}FeO_3$	5.566	13.709	424.71	0.546	19

a, b, c = lattice constants (Å), V = cell volume (Å^3), η = lattice strain, t = crystallite size (nm)

It is evident that the lattice parameters of BSFO nanostructures are found to be decreasing, and the lattice strain is found increasing with increasing concentration of Sc in BFO host up to 15%. This could be essentially attributed to the structural distortion occurred in BSFO nanostructures owing to the larger electronegativity difference of Sc-O (2.08) compared to Bi-O (1.42).[21] Accordingly, the observed shift in the doublet peaks of both particulates and fibers shown in Fig. 1(b) & 2(b) represents such substitution induced structural distortion in these BSFO nanostructures.

The larger electronegativity difference of Sc-O reduces the distance between Sc and O and lead to the structural distortion in the system which resulted in the modification of lattice parameters and induced the strain in the system.[21] The observed abrupt increment in crystallite size and decrement of strain in $Bi_{0.80}Sc_{0.20}FeO_3$ and $Bi_{0.75}Sc_{0.25}FeO_3$ particulate could be attributed to the composite like formation of the secondary phase $Bi_2Fe_4O_9$. This could also be corroborated with the observed relative drastic shift of doublet peaks (Fig. 1(b)) towards lower and higher 2Θ angle in $Bi_{0.80}Sc_{0.20}FeO_3$ and $Bi_{0.75}Sc_{0.25}FeO_3$ compositions, respectively. Where, the lower and higher 2Θ angle shift could be indirectly propositional to the concentration of this secondary in these BSFO compositions. In the case of fibers, the observed merging of doublet peaks (Fig. 2(b)) could be due to the structural changes in the system that could be attributed to their one-dimensional structure, which is also consistent with the existing reports.[22, 25]

3.2. Elemental and Chemical state analysis

The compositional and chemical state analyses of the fabricated compositions were carried out using X-ray photoelectron spectroscopy (XPS) technique. The obtained individual XPS spectra of Bi, Fe, O and Sc in the particulates and fibers of $Bi_{1-x}Sc_xFeO_3$, where x=0.0, 0.15 are shown in Fig. 3(a)-(d).

Figure 3(a) shows the XPS spectra of Bi 4f that consists of doublet peaks at around 158.26 and 163.60 eV that are corresponding to the binding energy (BE) of Bi–O bonds in pure BFO.[26] The two de-convoluted peaks at 156.96 and 162.72 eV are ascribed to Bi $4f_{7/2}$–O and Bi $4f_{5/2}$–O bonds, while other peaks fitted at 158.31 and 163.77 eV may be assigned to Bi–O–

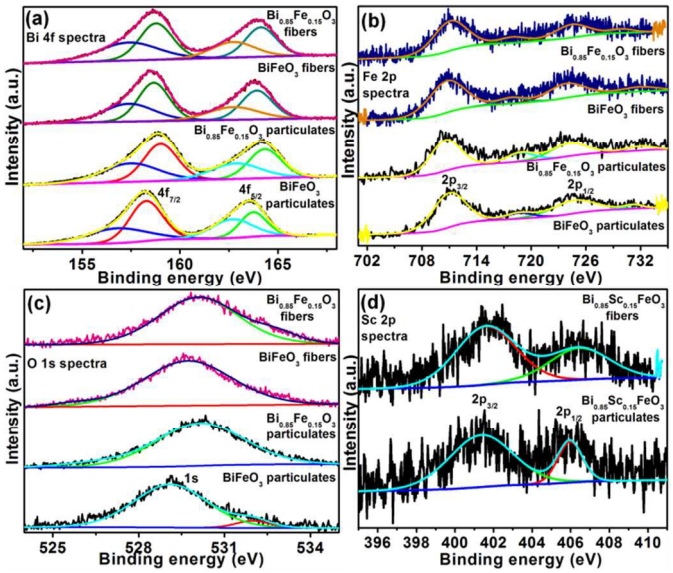

Fig. 3 XPS spectra of (a) Bi, (b) Fe, (c) O and (d) Sc in $Bi_{1-x}Sc_xFeO_3$ particulate and fiber nanostructures.

Fe bonds in oxygen octahedron and/or relaxed Bi phase. Further, the spin-orbit splitting energy (ΔE) of pure Bi 4f doublet is 5.34 eV, which is equivalent to theoretical value ($\Delta E_{\text{Bi 4f}}$) of 5.31 eV.[27] However, a chemical shift towards higher binding energy is observed in Bi 4f peaks with increasing concentration of Sc. This essentially shows that the occupancy of 'Sc' ions at the 'Bi' site in BFO host. The observed chemical shift could be elucidated based on the variation in ionicity of the compositions due to the substitution of Sc ions. The electronegativity of Bi, Sc, Fe and O is 2.02, 1.36, 1.83 and 3.44 respectively. The fraction of ionicity (Fi) of Bi-O, Sc-O and Fe-O bonds in BSFO nanostructures could be calculated from the equation, $Fi = 1\text{-}\exp(-(\Delta EN)^2/4))$, where ΔEN is the difference in electronegativities of anion and cation in the compositions.[28] According to the equation, the fraction of ionicity of Sc–O (0.66) is much higher than that of Bi–O (0.40), and binding energy of (Bi, Sc)–O bond in oxygen octahedron may be higher than that of ideal Bi–O bond, leading to the shift towards higher binding energy in the Bi 4f doublet peaks of BSFO nanostructures.

Figure 3(b) shows the Fe 2p spectra of pure BFO and BSFO nanostructures. The Fe 2p spectra of pure BFO show the doublet peaks at around 710.22 and 723.71 eV corresponding to Fe $2p_{3/2}$ and Fe $2p_{1/2}$ respectively, which can be due to Fe–O bonds.[26] The de-convoluted peaks at 711.32 and 725.67 eV could be assigned to (Fe $2p_{3/2})_2$–O_3 and (Fe $2p_{1/2})_2$–O_3 bonds, while the other peaks fitted at 710.11 and 724.10 eV may be associated with Fe–O–Bi bonds in oxygen octahedra and/or other relaxed Fe phase.[27,29] The calculated spin orbit splitting energy (ΔE) of pure Fe 2p doublet is 13.49 eV, which is found to be comparable with the theoretical value ($\Delta E_{\text{Fe 2p}}$) of 13.6 eV as in Fe_2O_3 system. This confirms that the Fe ions are existed

with the standard oxidation state of +3, which suggests the non-ionic defects nature in the compositions. This is because of the

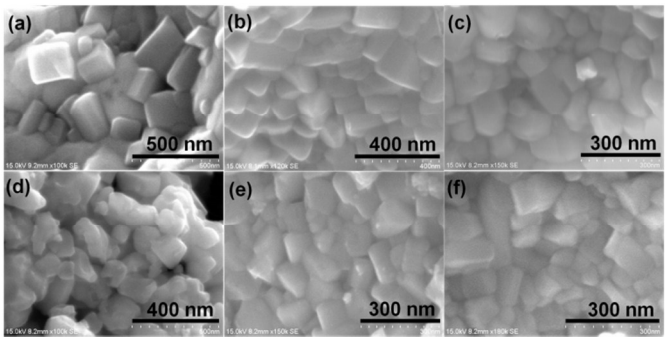

Fig. 4 FESEM image of $Bi_{1-x}Sc_xFeO_3$ particulate nanostructures, where (a) 0.0, (b) 0.05, (c) 0.10, (d) 0.15, (e) 0.20 and (f) 0.25.

fact that the Fe ions are volatile that switches between Fe^{3+} and Fe^{2+} states leading to the oxygen vacancies in the system. As observed in the case of Bi spectra, a shift towards higher binding energy is also observed in the case of Fe spectra with increasing concentration of Sc ions as in Fe-O-Bi(Sc) bonds.

The O 1s spectra of the particulate and fiber compositions are shown in Fig. 3(c) respectively. For pure BFO, the broad peak at 529.86 eV is corresponding to O 1s and the de-convoluted peaks at 529.27 and 531.99 eV could be assigned to the Bi–O 1s–Fe and the surface adsorbed oxygen species in the samples.[27] Considering Sc substituted BFO, the binding energy of O 1s in Sc-(O 1s) is higher than that of Bi-(O 1s) bonds and therefore the O 1s peak of the BSFO compositions shifts toward the higher binding energy as compared to pure BFO.

Figure 3(d) show the narrow scan XPS spectra of Sc in BSFO particulate and fiber compositions respectively. The doublet peaks at 401.47 and 405.97 eV corresponding to Sc $2p_{3/2}$ and Sc $2p_{1/2}$ as in the Sc_2O_3 system that confirms the +3 oxidization state of the substituted Sc ions in BSFO compositions.[25] The calculated spin-orbit splitting energy of the Sc 2p doublet is around 4.5 eV, which is well agreed with theoretical value of 4.4 eV.[27] The de-convoluted peaks at 401.92 and 406.72 eV could be assigned to Sc $2p_{3/2}$–O and Sc $2p_{1/2}$–O bonds for Sc $^{3+}$ ions, while the peaks at 399.57 and 404.56 eV may be associated with (Bi, Sc $2p_{3/2}$)–O and (Bi, Sc $2p_{1/2}$)–O bonds and/or relaxed Sc phase in the BSFO compositions. As observed in the XPS spectra of other elements, a gradual shift towards higher binding energy is also observed in the case of Sc that confirms the characteristic influence of substituted Sc ions in the BFO host.

3.3. Morphology analysis

The field emission scanning and high resolution transmission electron micrographs (FESEM and HRTEM) of the fabricated BSFO particulates nanostructures are shown in Fig. 4(a)-(f) and Fig. 5(a)-(f) respectively. Similarly, the FESEM and HRTEM images of BSFO fiber nanostructures are shown in Fig. 6(a)-(d) and Fig. 7(a)-(d) respectively.

The particle morphology was found to be cube like aggregated structures. The formation of such structure may be facilitated by citric acid, where it acted as a capping agent for the growth BFO particles with cube like morphology[30-34] as

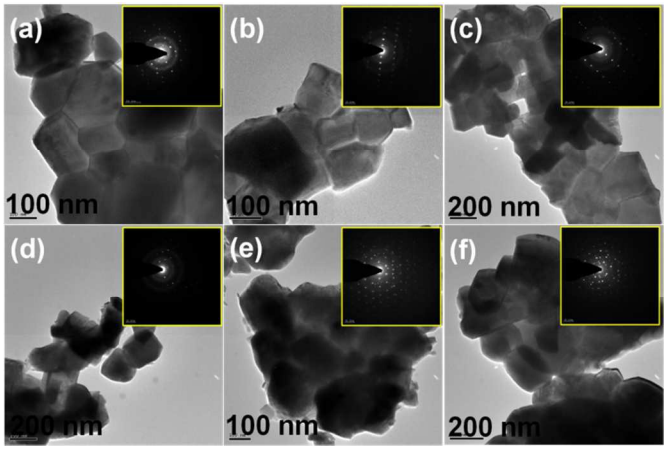

Fig. 5 HRTEM image of $Bi_{1-x}Sc_xFeO_3$ particulate nanostructures, where (a) 0.0, (b) 0.05, (c) 0.10, (d) 0.15, (e) 0.20 and (f) 0.25.

discussed and illustrated in Fig. S1, which is given in the Electronic Supplementary Information (ESI). It was observed from the micrographs that the average particle size is gradually reduced from 200 nm to 90 nm with increasing concentration of Sc from 0% to 25% in BFO host. This observed trend in the particle size reduction is in accordance with the crystallite size calculated from XRD pattern of the respective composition. Further, it should be noted that the morphology of the particle is not affected by the Sc substitution.

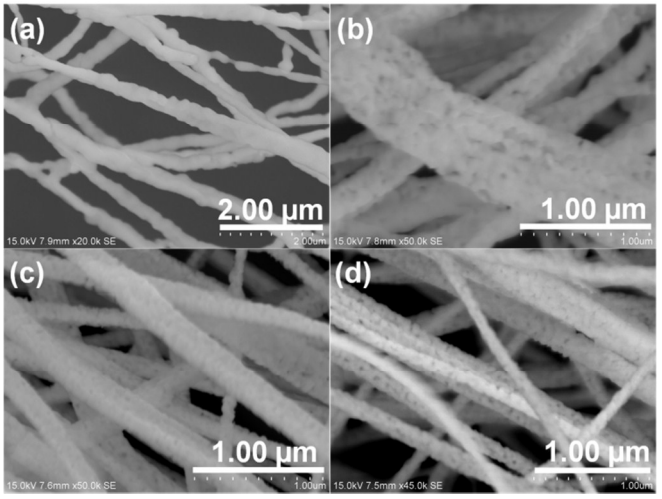

Fig. 6 FESEM image of $Bi_{1-x}Sc_xFeO_3$ fiber nanostructures, where (a) 0.0, (b) 0.05, (c) 0.10, and (d) 0.15.

As observed in the case of particulate system, the substitution induced size reduction is also consistent in Sc substituted BFO nanofibers as shown in Fig. 6(a)-(d) and Fig. 7(a)-(d). As mentioned that the manifestation of dimension dependent properties can be evidently distinguished while comparing 1-D and 3-D structures. Accordingly, the

substitution induced growth inhibition in BSFO fibers is evident where the growth of individual crystallites is significantly suppressed and it appears like a stack of inter-connected crystallites into one dimensional direction as

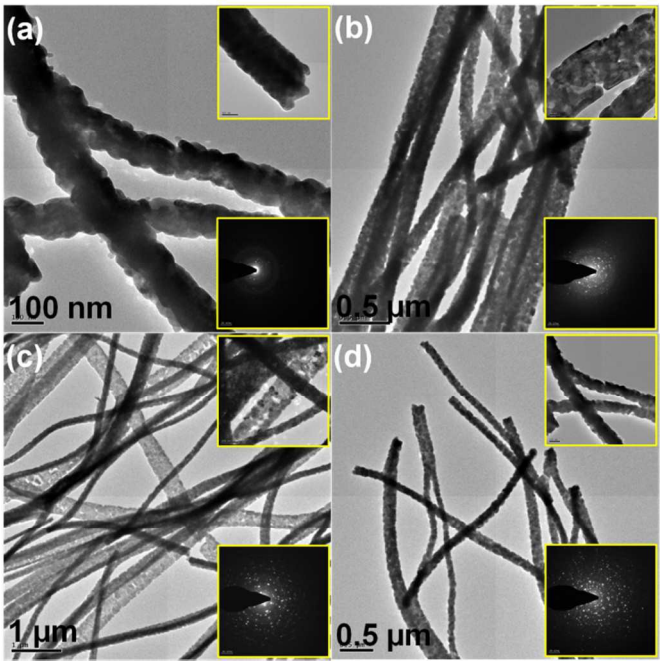

Fig. 7 HRTEM image of $Bi_{1-x}Sc_xFeO_3$ fiber nanostructures, where (a) 0.0, (b) 0.05, (c) 0.10, and (d) 0.15.

depicted in Fig. S2 given in the ESI. The average diameter of the fibers is found to be ~ 280 nm for pure BFO and it is reduced to 120 nm, 80 nm and 50 nm for $Bi_{(1-x)}Sc_{(x)}FeO_3$ where x=0.05, 0.10, 0.15 respectively.

We propose that such growth inhibition via substitution is possible when the deceleration in the site occupancy and subsequent nucleation of Sc ions in the Bi-Fe-O host. It can be understood that as the pure BFO solution contains only Bi and Fe ions where they effortlessly nucleate and subsequently grow as particles without any external interferences. But in the case of substitution, the substituted Sc ions may disturb the formation kinetics of BFO, as the phase should be formed along with the substituted Sc ions, which is likely a heterogeneous nucleation process. In the homogeneous mixture of Bi-Fe ions, the introduction of Sc ions is likely an impurity and causing anisotropicity that decelerates the nucleation as well as the subsequent growth of the particles. Such inducement of anisotropicity is mostly possible due to the smaller ionic radius of Sc^{3+} (0.92 Å) ions compared to Bi^{3+} (1.24 Å) ions.[21] It is therefore the increasing concentration of Sc in BFO host which increases the anisotropicity in the particle formation that leads to the suppression of particle growth as well as the formation of secondary phases as in the case of particulate system. In addition to this, the elemental analysis of these fabricated particulate and fiber nanostructures was also carried out by using energy dispersive X-ray spectroscopy (EDS) technique and the obtained EDS spectra are shown Fig. S3 and S4, respectively in the ESI.

3.4. Estimation of band gap energy

The optical absorption characteristics of the fabricated $Bi_{1-x}Sc_xFeO_3$ particulate (where x = 0, 0.05, 0.10, 0.15, 0.20, 0.25),

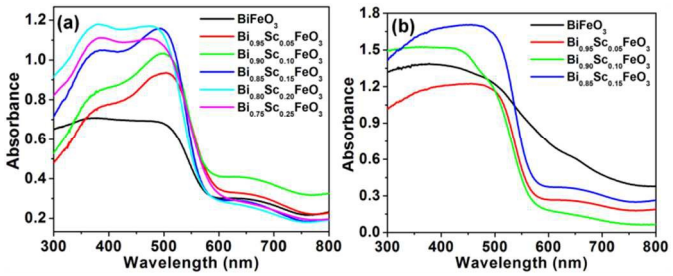

Fig. 8 UV-Visible absorption spectrum of $Bi_{1-x}Sc_xFeO_3$ (a) particulates and (b) fiber nanostructures.

and fiber (where x = 0, 0.05, 0.10, 0.15) nanostructures is deduced from their UV-Visible absorption spectra as shown in Fig. 8(a)-(b), respectively, where the band gap energy is calculated from their diffuse reflectance spectra using Kubelka-Munk function,[35] which is given in Fig. S5(a)-(f) and Fig. S6(a)-(d) of ESI.

From the graphs, the observed red shift in the absorption peaks of BSFO compositions essentially signifies that the Sc substitution enhances the visible light absorption of BFO. Correspondingly, the band gap energy is found decreasing with increasing concentration of Sc in both BFO particulate and fiber system. The band gap values are listed in Table 2. According to a DFT study, it was observed that the substitution of Sc significantly reduced the band gap energy of BFO.[21] The mechanism for observed band gap reduction was attributed to the following factors: (i) the stronger hybridization of Sc-O and (ii) the Fe-O-Fe super-transfer mechanism. This can be explained as follows. In the band gap structure of BFO, the Bi 6*p*/6*s*, Fe 3*d*, and O 2*p* states are present both in conduction band (CB) and valence band (VB) of BFO. Also, the transfer of Fe 3*d* electrons is mediated by the O 2*p* states and not directly between the 3*d* states. Therefore, any influence in the band gap structure of BFO involves the contribution of the both Bi and Fe ions and their amalgamation with O 2*p* states.

Accordingly, in our case, the stronger hybridization between Sc-O owing to the large electronegativity difference reduced its inter-atomic distances and it ultimately resulted in the wider dispersion of bands and the band gap reduction. Further, as the transfer of Fe 3*d* electrons is mediated by O 2*p* states, it established the Fe-O-Fe super-transfer process where the 3*d* states of both Fe and Sc together overlapped with O 2*p* states and leads the band gap reduction in BSFO nanostructures.

Table 2. Estimated band gap energy of the $Bi_{1-x}Sc_xFeO_3$ nanostructures.

Particulates		Fibers	
Composition	*Bandgap (eV)	Composition	*Bandgap (eV)
$BiFeO_3$	2.36	$BiFeO_3$	2.42
$Bi_{0.95}Sc_{0.05}FeO_3$	2.31	$Bi_{0.95}Sc_{0.05}FeO_3$	2.34
$Bi_{0.90}Sc_{0.10}FeO_3$	2.29	$Bi_{0.90}Sc_{0.10}FeO_3$	2.33
$Bi_{0.85}Sc_{0.15}FeO_3$	2.26	$Bi_{0.85}Sc_{0.15}FeO_3$	2.31
$Bi_{0.80}Sc_{0.20}FeO_3$	2.21	-	-
$Bi_{0.75}Sc_{0.25}FeO_3$	2.24	-	-

*Calculated from DRS spectra (shown in ESI) using Kubelka-Munk function.

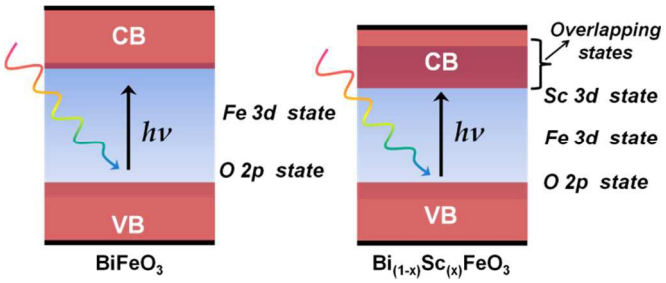

Fig. 9 Concept of the observed band gap reduction in $Bi_{1-x}Sc_xFeO_3$ nanostructures.

The concept of overlapping enabled band structure dispersion and band gap reduction is illustrated in Fig. 9. On the other hand, the observed abrupt band gap reduction in $Bi_{0.80}Sc_{0.20}FeO_3$ and $Bi_{0.75}Sc_{0.25}FeO_3$ particulates could be attributed to the existence of secondary phase in these compositions.

3.5. Magnetic properties analysis

TEMPERATURE DEPENDENT MAGNETIC PROPERTIES: The magnetic measurements of the fabricated pure and Sc substituted BFO particulate and fiber nanostructures were carried out by super conducting quantum interference device (SQUID) magnetometer. All the samples were characterized for their temperature dependent (5 K to 300 K, at 100 Oe) zero-field cooling (M_{ZFC}) and field cooling (M_{FC}) magnetization as well as magnetic hysteresis (M-H) at room temperature (300 K) and at low temperature (5 K).

Figures 10(a)-(f) show the ZFC and FC magnetization curves of $Bi_{1-x}Sc_xFeO_3$ (where x = 0, 0.05, 0.10, 0.15, 0.20, 0.25) particulate nanostructures. In the curves, there are significant observations, which essentially reflect the origin of enhanced magnetic properties in the BSFO particulate nanostructures; (i) the splitting of ZFC and FC curves and (ii) with decreasing temperature from 300 to 5 K, the ZFC magnetic moment (M_{ZFC}) slightly increases then monotonically decreases for pure BFO, while it significantly increases then decreases and leads to the appearance of a broad peak in the ZFC curves for the Sc substituted BFO compositions. The above facts can be interpreted as follows. It is known that the typical BFO is antiferromagnetic (AFM) material which often shows weak ferromagnetism (FM) when the particle size is reduced to nanoscale.

Accordingly, (i) the observed splitting of ZFC and FC curve is essentially due to the coexistence of AFM and FM ordering in the system.[36] Further, it can also be due to the other factors such as enhanced canted AFM spin structures owing to the particle size effects.[37] (ii) The initial increment in the M_{ZFC} with decreasing temperature and the plateau like region in the FC curve in lower temperatures indicate the existence of interacting superparamagnetic behaviour in the nanostructures (superparamagnetism is the size effect of ferromagnetism).[25,38]

On the other hand, the appearance of broad peak associated with the decrement in M_{ZFC} at lower temperatures indicates the blocked state of superparamagnetic ordering in these

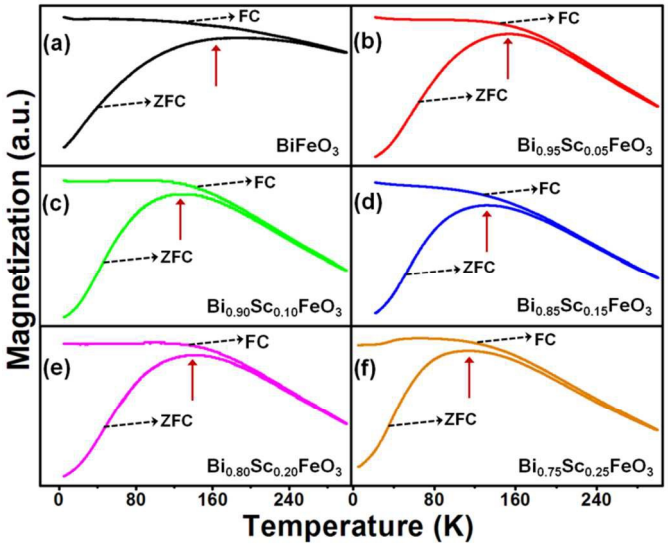

Fig. 10 Temperature dependent magnetization (FC-ZFC) of $Bi_{1-x}Sc_xFeO_3$ particulate nanostructures.

Nanostructures.[39] In the superparamagnetic particles, as their magnetic moment along any one of the anisotropic directions is blocked at the temperatures below blocking temperature (T_B) (indicated with an arrow mark), they do not respond to the small applied field (here it is 100 Oe). For this reason, below the T_B, the changes in the magnetization values are minimal with increase in temperature in the case of FC curves. While in the case of ZFC curves, the magnetization value tend to increase with increasing temperature. Furthermore, the presence of distribution in the blocking temperature (appeared like a plat peak rather than the sharp peak) leads to the splitting of M_{ZFC} and M_{FC} to start slightly lower than T_B, which can be observed in both pure and Sc substituted BFO.[25] A thermo-magnetic irreversibility can also be seen from the unambiguous separation of M_{ZFC} and M_{FC} curves. This thermo-magnetic irreversibility signifies the initiation of blocking process which is essentially induced by the dissonance between the magneto-crystalline anisotropy and thermal activation energy in the particulate system.[40]

The ZFC and FC magnetization curves of $Bi_{1-x}Sc_xFeO_3$ (where x = 0, 0.05, 0.10, 0.15) fiber nanostructures are shown in Fig. 11(a)-(d), respectively. As observed in the particulate system, the typical splitting of ZFC and FC curves indicates the

co-existence of AFM-FM phases in both pure and Sc substituted BFO nanofibers. However, the ZFC magnetization profile of fibers is found to be distinctively different compared to particulate nanostructures.

For pure, 5% and 15% Sc substituted BFO, the ZFC magnetic moment is monotonically decreasing with decreasing temperature without exhibiting any peak corresponding to blocking temperature. In nanomaterials, due to the size induced magnetic anisotropy, the magnetic moment has only two stable orientations which are anti-parallel to each other, separated by an energy barrier.[41] In such circumstances, at particular temperature there is a finite possibility for the magnetization to

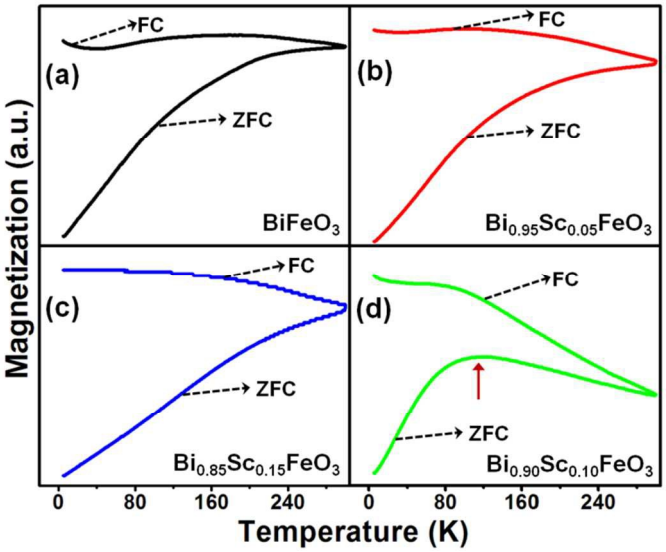

Fig. 11 Temperature dependent magnetization (FC-ZFC) of $Bi_{1-x}Sc_xFeO_3$ fiber nanostructures.

flip and reverse its direction. The mean time between the two flips is called the Neel relaxation time (τ_N).[42] The prolonging of this τ_N for some time indicates the frozen state of the spins that turns the magnetic materials to the blocked state. This Neel relaxation time as function of temperature is corresponding to the T_B which can be obtained from the ZFC curves. The magnetic state of material before reaching T_B is likely superparamagnetic and after T_B is the blocked state.[43] As observed in our BFO fiber system, this T_B is likely to appear in the room temperature itself where there is a consistent fall in the magnetic moment with decreasing temperature. This implies that the ferromagnetic ordering persists in pure, 5% and 15% Sc substituted BFO fiber nanostructures. Accordingly, the existence of superparamagnetic nature can also corroborated with the observed saturation behaviour in the room and low temperature *M-H* hysteresis curves of these materials. Conversely, a typical AFM-FM behaviour was observed in the case of 10% Sc substituted BFO nanofibers which can also be corroborated with its room and low temperature *M-H* curve exhibiting the AFM nature of possessing lower magnetization values. This may be due to the induction of some magnetic anomalies due to the lack of contribution of Sc ions in the magnetic properties of $Bi_{0.90}Sc_{0.10}FeO_3$ nanofibers. As illustrated in Fig. 12, the emergence of spin canted structure is enhanced by Sc^{3+} ions in BSFO nanostructures. Therefore it is expected that the distribution of Sc^{3+} ions in $Bi_{0.90}Sc_{0.10}FeO_3$ nanofibers may be inhomogeneous and their contribution in the spin canting structures is nominal which eventually lowered the net magnetic moment in the system. Nevertheless, such inconsistency can also be seen in the photocatalytic activity of this particular composition which is discussed in the following section.

Therefore, the observed net magnetic moment in the pure and Sc substituted BFO system and the splitting phenomenon of ZFC and FC curves owe their origin to the existence of

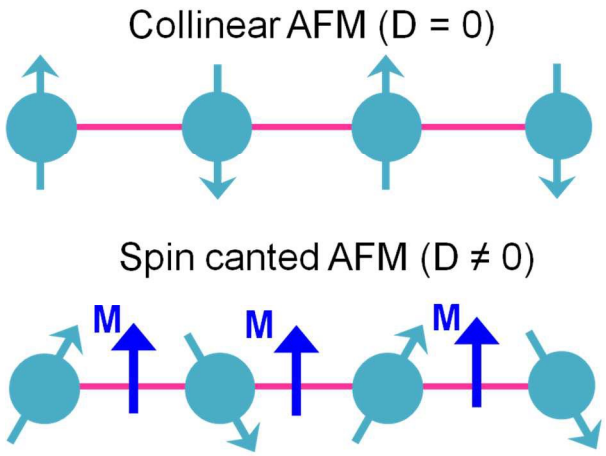

Fig. 12 Manifestation of 'canted' spin structure induced net magnetic moment in the BSFO nanostructures due to Dzyaloshinskii-Moriya (DM) interactions.

AFM-FM phase and 'the canted' spins in the surface of the particles. It is understood that even if the induced ferromagnetic nature becomes predominant in BSFO, its inherent AFM ordering cannot be eliminated from the system.

MAGNETIC HYSTERESIS PROPERTIES: Figure 13 (a)-(d) and Fig. 14 (a)-(d) shows the room (300 K) and low temperature (5 K) magnetic hysteresis (M-H) curves of $Bi_{1-x}Sc_xFeO_3$ particulate (where x = 0, 0.05, 0.10, 0.15, 0.20, 0.25), and fiber (where x = 0, 0.05, 0.10, 0.15) nanostructures, respectively at a maximum applied field of 2T.

The hysteresis curve of pure BFO particulate and fiber nanostructures clearly indicates the manifestation of weak ferromagnetic nature in contrast to a typical bulk BFO which exhibits antiferromagnetic (AFM) properties. This could be due to the smaller crystallite size of pure BFO which may result, (i) the suppression of cycloidal spin structure in BFO or (ii) the formation of AFM-core/FM-shell like structure due to the uncompensated electrons spins in one sublattice by another sublattice in smaller AFM-BFO crystals. Accordingly, the conception of AFM/FM core/shell structure could be substantiated by associating with the observed displacement in the *M-H* curve of pure BFO as shown in the Fig. 13(b) & (d) and Fig. 14(b) & (d), which is consistent with other literature reports. [25, 36, 44-45]

On other hand, this weak ferromagnetic nature is significantly enhanced due to the Sc substitution in BFO.

Accordingly, the observed enhancement in the BSFO particulate and fiber nanostructures could be essentially attributed to the substitution induced structural disorder and the modified 'canted' spin structure due to the Fe-O-Fe interaction in host BFO rather than the AFM/FM core/shell phenomenon. This is because, the displacement in the *M-H* curve as observed for pure BFO NPs do not occur in Sc substituted BFO NPs as well as NFs (including pure BFO NFs). In general, the exchange interaction between AFM and FM induces the unidirectional anisotropy that leads to the shift along the magnetic field axis in the *M-H* hysteresis curve. This effect is known as exchange bias (EB).[46]

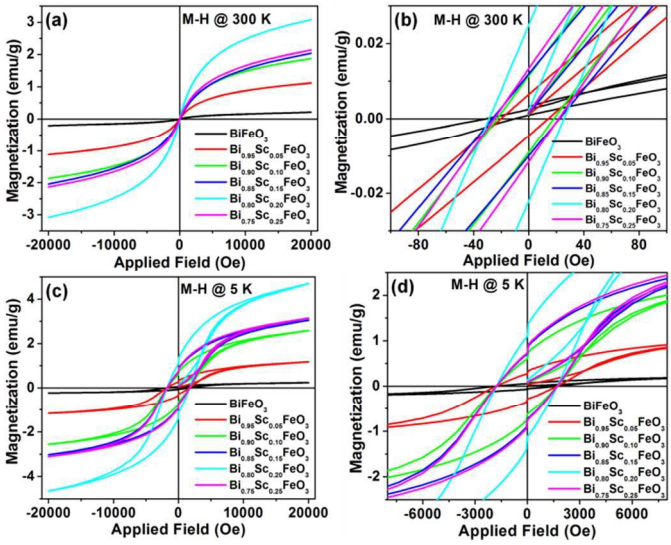

Fig. 13 Field dependent magnetic hysteresis (*M-H*) curves of $Bi_{1-x}Sc_xFeO_3$ particulate nanostructures at (a)-(b) 300 K and (c)-(d) 5 K.

It is proposed that the emergence of EB is due to the existence of uncompensated spins in the system.[47] However, it is also possible for EB to emerge in a system consisting of compensated spins, where the 'canted' spin structures lead to the enhancement in the magnetic properties rather than the uncompensated spins.[48] Such a system can be explained by Dzyaloshinskii-Moriya (DM) interactions.[49] The fundamental idea of DM interaction is the induction of magnetization in antiferromagnets due to the modification in 'canted' spins as a result of the ferroelectric distortions.[50] Therefore we suggest that the emerged ferroelectric distortion in BSFO system modified its 'canted' spin structure (Fe-O-Fe) and lead to an enhanced magnetic properties as illustrated in Fig. 12. It is noteworthy that the observed phenomenon is also known as 'ferroelectrically-induced ferromagnetism' which is generally originated due to this DM interaction in BFO.[51] Accordingly, both particulate and fiber nanostructures showed an enhanced magnetic hysteresis properties at low temperature, which is shown in Fig. 13(c) and 14(c).

Further, in the case of BSFO particulate system, it can be seen that a drastic enhancement in the magnetic property of $Bi_{0.80}Sc_{0.20}FeO_3$ and a fall in $Bi_{0.75}Sc_{0.25}FeO_3$ composition. It is presumed that these anomalies might be due to the existence of the secondary phase ($Bi_2Fe_4O_9$) at higher and lower concentrations, respectively. Accordingly, the intensity of the XRD peaks corresponding to this secondary phase and the shift in doublet peak is found to be pronounced due to the higher concentration of $Bi_2Fe_4O_9$ phase in $Bi_{0.80}Sc_{0.20}FeO_3$ compared to $Bi_{0.75}Sc_{0.25}FeO_3$ composition. Moreover, the doublet peak of $Bi_{0.75}Sc_{0.25}FeO_3$ composition is found to be shifted towards higher 2Θ angle as the trend observed in the rest of compositions, which is probably attributed to the lower concentration of $Bi_2Fe_4O_9$ phase. Further, this conception can also be corroborated with the observed enhancement in their optical properties. In addition to this, an independent study on $Bi_2Fe_4O_9$ also reports that the $Bi_2Fe_4O_9$ is magnetically active

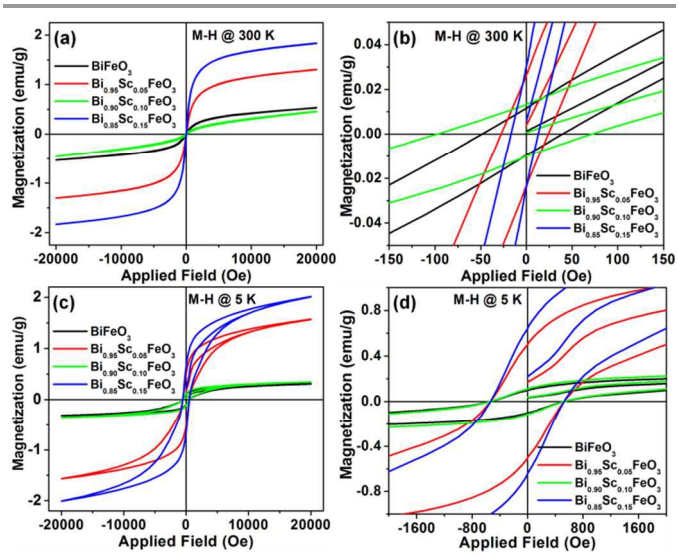

Fig. 14 Field dependent magnetic hysteresis (*M-H*) curves of $Bi_{1-x}Sc_xFeO_3$ fiber nanostructures at (a)-(b) 300 K and (c)-(d) 5 K.

and that it tends to exhibit the coexistence of AFM-FM phases as similar to $BiFeO_3$.[52]

Therefore we believe that the concentration of the secondary phase might give a rise and fall in the magnetic properties of $Bi_{0.80}Sc_{0.20}FeO_3$ and $Bi_{0.75}Sc_{0.25}FeO_3$ compositions, respectively. The observed values of the magnetic parameters such as saturation magnetization (M_s), remnant magnetization (M_r), coercive field (H_c) and blocking temperature (T_B) of particulate and fiber nanostructures are given in the Table 3.

Table 3 Obtained magnetic parameters of the $Bi_{1-x}Sc_xFeO_3$ nanostructures

	*M_s (emu/g)		M_r (emu/g)		H_c (Oe)		T_B
	300 K	5 K	300 K	5 K	300 K	5 K	(K)
Particulates ($Bi_{1-x}Sc_xFeO_3$)							
0.00	0.21	0.23	0.002	0.01	32	199	172
0.05	1.12	1.61	0.006	0.45	20	1911	145
0.10	1.87	2.93	0.011	0.79	23	2037	129
0.15	2.04	3.48	0.012	0.83	26	1935	122
0.20	3.08	4.71	0.025	1.11	29	1778	141
0.25	2.14	3.52	0.011	0.37	25	781	113
Fibers ($Bi_{1-x}Sc_xFeO_3$)							
0.00	0.53	0.41	0.011	0.09	48	853	-
0.05	1.31	1.34	0.026	0.41	27	756	-
0.10	0.46	0.50	0.013	0.10	97	1130	120
0.15	1.84	1.93	0.030	0.76	17	818	-

*Magnetic saturation (M_s) at 2 T

3.6. Photocatalytic properties

The photocatalytic efficiency of the fabricated pure BFO and BSFO particulate and fiber nanostructures on the degradation of methylene blue (MB) dye was studied under the direct exposure of sunlight. Individual degradation spectra of $Bi_{1-x}Sc_xFeO_3$ particulate (where x = 0.0, 0.05, 0.10, 0.15, 0.20, 0.25) and fiber (where x = 0.0, 0.05, 0.10, 0.15) are shown in Fig. S7 (a)-(f) and S8 (a)-(d), respectively (given in the ESI) and their C/C_0 ratio graphs and final degradation percentage graphs are shown in Fig. 15(a)-(d), respectively. As it can be seen in the C/C_0

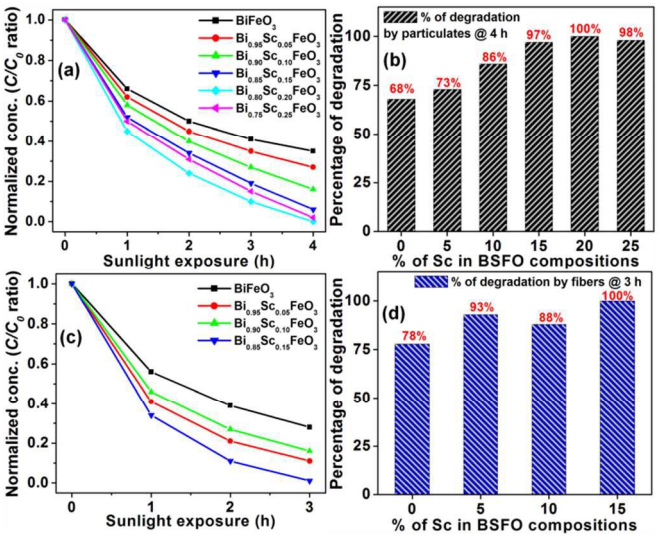

Fig. 15 Photocatalytic efficiency graph (C/C_o ratio) and degradation percentage of $Bi_{(1-x)}Sc_{(x)}FeO_3$ (a)-(b) particulate and (c)-(d) fiber nanostructures.

graph (Fig. 15 (a) & (c)), the photocatalytic degradation is found increasing with increasing concentration of Sc in BFO, except $Bi_{0.75}Sc_{0.25}FeO_3$ particles and $Bi_{0.90}Sc_{0.10}FeO_3$ fibers. It is noteworthy that the photocatalytic efficiency of nanofibers is found to be enhanced compared to particulate nanostructures. This is that the average time taken by the particulates and fibers to degrade the given amount of dye is found to be 4 h and 3 h, respectively. Accordingly, at the end of 4 h of sunlight irradiation, BSFO particulates (where x = 0.0, 0.05, 0.10, 0.15, 0.20, 0.25) degraded around 69%, 73%, 86%, 97%, ~100%, 98% of the dye respectively. In the case of BSFO fibers (where x = 0.0, 0.05, 0.10, 0.15), the degradation percentage is found to be around 78%, 93%, 88%, ~100%, respectively at the end of 3 h.

The observed photocatalytic efficiency of these nanostructures can be discussed in two perspectives. One is the dimension and another is the influence of Sc substitution in these BFO particulate and fiber nanostructures. Accordingly, the observed efficiency in the 1-D fibers of BFO could be directly ascribed to the synergic effect resulting from their confined and unconfined dimensions. The unfettered dimension of these 1-D materials essentially decreases the recombination probabilities of photo-generated charge carries (e^-/h^+) due to the enhanced recombination resistance in these fiber nanostructures,[43-54] whereas, the fettered direction influences the charge transferring mechanisms due to the formation of discrete energy levels as a result of the confinement. In the 1-D materials, once the charge-separation is established in the system, the electrons excited to the conduction band (CB) get delocalized as they diffuse into the their wide bandwidth dispersion. Eventually, it delays the recombination possibilities of charge carriers in these 1-D materials.[55] Under such circumstances, the energy applied for charge separation is sustained in the system and utilized for the production of redox species in the medium that leads to the effective degradation of dye molecules.

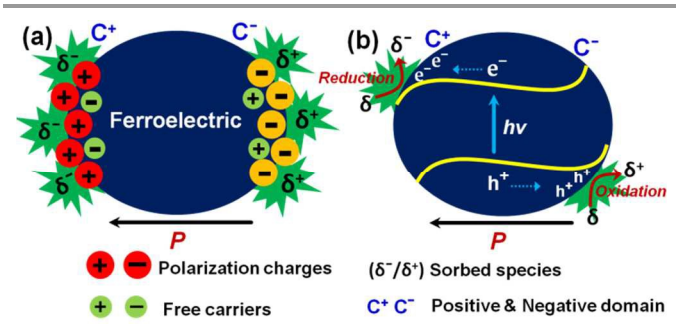

Fig. 16 (a) The spontaneous polarization in ferroelectrics and charge compensation mechanism, and (b) band-bending phenomenon induced charge carriers transportations in a ferroelectric material.

On the other hand, the photocatalytic enhancement due to the Sc substitution in BFO nanostructures could be attributed to the following factors; (i) effect of reduced band gap, and (ii) substitution induced band bending phenomena. As discussed, the observed reduction in the band gap energy with increasing concentration of Sc in BFO lead to the absorption of more visible light energy which expedited the photocatalytic process in these BSFO nanostructures. In the perspective of BFO as a 'ferroic-semiconductor', its ferroelectricity induced band bending phenomenon is an appealing feature that essentially favours the photocatalytic process in BFO in many different ways.[54,58] In ferroelectric materials, the off-centre displacement of positive and negative ions causes the spontaneous polarization and thereby it induces macroscopic charges on their surfaces.[16,58] The spontaneous polarization produces positively (C^+ domains) and negatively (C^- domains) charged

surfaces when the direction of the spontaneous polarization points from bulk to surface and surface to bulk, respectively. However, these induced charges on the surface will be compensated by unbound charge carriers (e^-/h^+) and defects in the volume of ferroelectric materials and/or by the surface-adsorbed charged molecules (δ^+/δ^-) from the surrounding medium. During such charge compensation process, the electrons will be moved towards the surface of C^+ domains leading to downward band bending. Conversely, in C^- domains, the free electrons will be moved away from the surface, resulting in upward band bending. The formation of C^+, C^- domains and the band bending phenomena are illustrated in Fig. 16 (a)-(b).[16]

This band bending in ferroelectric photocatalytic materials helps in the inhabitation of carrier recombination and creates a pathway for the transfer of charge carriers to the surface of photocatalyst. When a light energy falls on the ferroelectric-semiconductor, the exciton pairs (e^-/h^+) will be generated where the negative electrons move to the conduction band (CB) leaving positive holes in the valence band (VB). Once charge separation is sustained, the electron and hole may migrate to the catalyst surface where they get involved in redox reactions with sorbed species.[59] Especially, the holes (h^+) in the VB may react with surface-bound H_2O or OH^- to produce the hydroxyl radical and the electrons (e^-) in the CB are picked up by oxygen

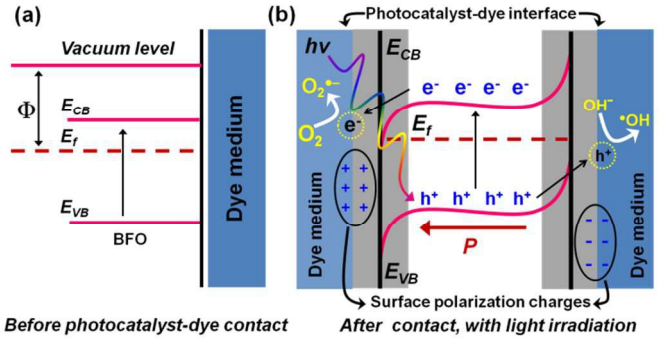

Fig. 17 Band structures in BFO (a) before and (b) after its contact with dye; where the transportation of carriers being is facilitated via band bending process due to their multiferroic-ferroelectric properties.

to generate superoxide radical anion ($O_2^{\bullet-}$), as indicated in the following Equations 1–3:

Absorption of efficient photons by photocatalyst

$BiFeO_3 + hv \rightarrow e^-_{cb} + h^+_{vb}$ (1)

Formation of superoxide radical anion

$O_2 + e^-_{cb} \rightarrow O_2^{\bullet-}$ (2)

Neutralization of OH^- group into $^\bullet OH$ by the hole

$OH^- + h^+_{vb} \rightarrow {}^\bullet OH + H^+$ (3)

The hydroxyl radical ($^\bullet OH$) and superoxide radical anions ($O_2^{\bullet-}$) are the primary oxidizing species in the photocatalytic oxidation processes. These oxidative reactions would cause the degradation of the pollutants as shown in the following Equations 4 and 5:

Oxidation of the dye via successive attack by $^\bullet OH$ radicals

Dye + $^\bullet OH \rightarrow$ Dye'$^\bullet$ + H_2O (4)

Or by direct reaction with holes

Dye + $h^+_{vb} \rightarrow$ Dye$^\bullet$ + $\rightarrow$ degradation products (5)

Accordingly, the emerged band bending in BSFO nanostructures creates a pathway for the excited electrons (in CB) and holes (in VB) to drive to photocatalyst-dye interface as illustrated in Fig. 17 (a)-(b), and lead the carriers to the reduction and oxidation process, respectively. Thereby, a ferroelectric material can enhance the photocatalytic process by separating the electron and holes owing to its internal electrical field associated with the induced asymmetricity in the crystal system.

As discussed above that the substitution of Sc^{3+} ions caused a structural distortion in the system through the off-displacement of octahedral cage resulted in enhanced ferroelectric properties. Therefore, the observed photocatalytic efficiencies can be attributed to the band bending phenomena emerged due to the spontaneous ferroelectric properties in BSFO nanostructures. The enhancement in the ferroelectric properties in these compositions can be correlated to the observed enhancement in their magnetic properties as it is attributed to the 'ferroelectrically-induced ferromagnetism'. Further, it is noteworthy that the $Bi_2Fe_4O_9$ is also a photocatalytic material[60] and therefore we believe that the presence of this secondary phase in $Bi_{0.80}Sc_{0.20}FeO_3$ and $Bi_{0.75}Sc_{0.25}FeO_3$ compositions might have also contributed in their photocatalytic enhancements. Similarly, the observed

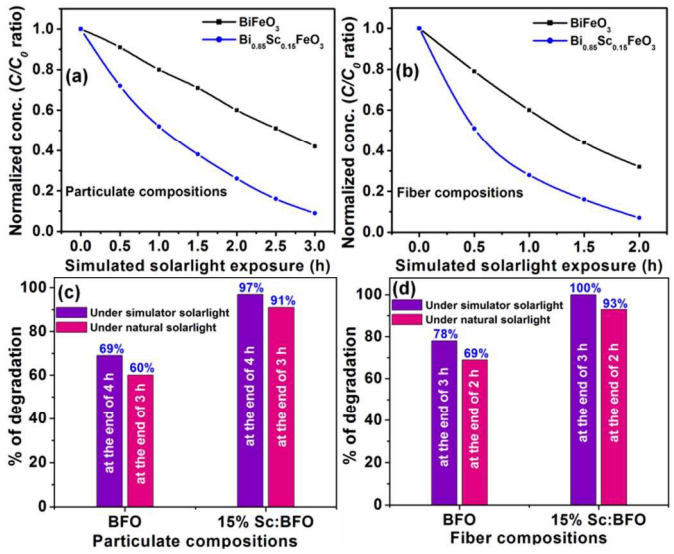

Fig. 18 Photocatalytic efficiency of pure and 15% Sc: BFO (a) particulate and (b) fiber nanostructures under simulator solar light; (c)-(d) comparative bar diagram representing the degradation percentages under natural and simulated solar light irradiation.

decrement in the photocatalytic activity of $Bi_{0.90}Sc_{0.10}FeO_3$ nanofibers could be attributed to the anomalies associated with the carrier density in the material. For instance, it is reported that, in heavily doped semiconductors, the attractive Coulomb interaction between electrons and holes itself vanishes at e^-/h^+ densities in the form of excitons.[61,62] In the PC process, the

charge separation is crucial factor to observe an enhanced PC activity. Therefore, the observed decrement in the PC activity of $Bi_{0.90}Sc_{0.10}FeO_3$ nanofibers could be attributed to the race between the formation of excitons and charge separation.

For a comparative study, the photocatalytic activities of pure as well as 15% Sc substituted BFO particulate and fiber nanostructures were investigated under the simulated solar light. It can be seen that the degradation under simulated solar light is found to be enhanced as compared to that of the degradation obtained under natural sunlight. From the obtained C/C_0 ratio graphs as shown in Fig. 18 (a)-(b), the pure BFO and $Bi_{0.85}Sc_{0.15}FeO_3$ particulates degraded around 69 % and 97 % of the dye at the end of 4 h under natural sunlight. Whereas, under the simulated solar light, it took 3 h to degrade the nearly the same amount of dye 60 % and 91%. Similarly, pure BFO and $Bi_{0.85}Sc_{0.15}FeO_3$ fibers degraded 69 % and 93 % of the dye at the end of 2 h under simulated solar light, while it was 78 % and 100 % at the end of 3 h under the natural sunlight irradiation, which are depicted as the bar diagrams shown in Fig. 18(c)-(d). The obtained degradation time difference could be due to the intensity and the thermal energy associated with the simulated solar light source. However, it is essentially to show that the photocatalytic degradation under natural sunlight is rational as compare to the simulated solar light sources. Further, the photocatalytic recyclability tests were also carried out for some selected particulate and fiber compositions (pure $BiFeO_3$, $Bi_{0.95}Sc_{0.05}FeO_3$ and $Bi_{0.85}Sc_{0.15}FeO_3$) under the natural solar light. The obtained results are shown in Fig. S9(a)-(b) of ESI. Form the recyclability experiments, the fiber compositions showed relatively enhanced stability as compared to the particulates. This is because of the fact that the fibers tend to be stoichiometrically ideal (which could be corroborated from their XPS analysis) as compared to that of the particulates. Moreover, in terms of the recovery process, the fibers tend to be easy to recover without any loss as compared to the particulates.

4. Summary and Conclusion

$Bi_{1-x}Sc_xFeO_3$ (BSFO) particulate (where x = 0.0, 0.05, 0.10, 0.15, 0.20, 0.25) and fiber (where x = 0.0, 0.05, 0.10, 0.15) nanostructures were fabricated by sol-gel and electrospinning methods, respectively. Influence of Sc substitution in these nanostructures was studied on the structural, morphological, optical, temperature dependent magnetic and sunlight driven photocatalytic properties. The substitution of Sc in BFO essentially caused the structural distortion in the system due to its smaller ionic radius. Such structural modification led to the reduction in crystallite size and increment in strain of the system which was evident from their XRD patterns. From the FESEM and HRTEM micrographs, the morphology of BSFO particulate nanostructures was found to be cube like aggregated structures. The size of the particulate and fiber nanostructures was found to be decreased with increasing concentration of Sc in BFO host. The band gap energy in BSFO compositions was considerably reduced and it was attributed to the strong overlapping of Sc 3*d* sates with O 2*p* states along with Fe 3*d* states in BSFO nanostructures. Temperature dependent magnetic properties, i.e. FC-ZFC curves suggested that the origin of magnetic property in pure BFO particulates and fibers was due to the existence of AFM/FM core/shell structure, while it was due to the modified spin 'canted' structures (Dzyaloshinskii-Moriya interactions) in the case of BSFO nanostructures. Accordingly, the room temperature and low temperature magnetic hysteresis curves showed an enhanced magnetization with increasing concentration of Sc in BFO. Despite the magnetization values being low for the fiber systems compared to particulates, the observed saturation trend signified the existence of a relatively stable ferromagnetic alignment in BSFO nanofibers. It was observed from the photocatalytic (PC) studies that the BSFO nanofibers degraded the given amount of dye one hour earlier than particulates. This was attributed to the dimension dependent PC properties, in which the excited electrons in the fibers were likely delocalized in their conduction band and reduced recombination possibilities; thereby it enhanced the PC activity. Further the band bending process enhanced the charge compensation process and facilitated the promotion of excited carriers to the catalyst-dye interfaces; thereby this process led to an efficient and faster degradation of dye molecules under the sunlight irradiation. The photocatalytic degradation under simulated solar light source was found to be faster compared to the degradation under natural sunlight. However, the results obtained suggested that the efficiency of the photocatalyst under sunlight irradiation is rational compared to simulated solar light source. The photocatalytic recyclability tests revealed the better catalytic stability of fibers compared to the particulates.

Acknowledgements

Authors gratefully acknowledge the Council of Scientific and Industrial Research (CSIR) for funding support (80(0074)/10/EMR-II, dt. 30-12-2010), and one of the authors, M. Sakar gratefully acknowledges the NCNSNT-MHRD for the postdoctoral research fellowship (C-2/NSNT/pdf/2014/044, dt. 24-01-2014), to carry out this research work.

Notes and references

[a,*]National Centre for Nanoscience and Nanotechnology, University of Madras, Guindy campus, Chennai 600025, India. Fax: 044-22352494/ 22353309; Tel: 044-22202749, *E-mail: balasuga@yahoo.com.
[b]Defence Metallurgical Research Laboratory, Hyderabad 500058, India.

1. M. Bibes, A. Barthelemy, *Nature Mater*., 2008, **7**, 425.
2. (a) N. A. Spaldin, M. Fiebig, *Science,* 2005, **309**, 391. (b) M. Fiebig, *J. Phys. D: Appl. Phys*., 2005, **38**, R123.
3. (a) A. Nicola Hill; *J. Phys. Chem. B,* 2000, **104**, 6694 (b) Liliana Mitoseriu, *Bol. Soc. Esp. Ceram. V*., 2005, **44**, 177.
4. (a) P. Fischer, M. Polomska, I. Sosnowska, M. Szymanski, *J. Phys. C: Solid State Phys*., 1980, **13**, 1931.

5. (a) R. Ramesh, N. A. Spaldin, *Nat. Mater.,* 2007, **6**, 21. (b) S. W. Cheong, M. Mostovoy, *Nat. Mater.,* 2007, **6**, 13. (c) W. Eerenstein, N. D. Mathur, J. F. Scott, *Nature,* 2006, **442**, 759.
6. Z. X. Cheng, X. L.Wang, Y. Du, S. X. Dou, *J. Phys. D: Appl. Phys.,* 2010, **43**, 242001.
7. C. H. Yang, D. Kan, I. Takeuchi, V. Nagarajan, J. Seidel, *Phys. Chem. Chem. Phys.,* 2012, **14**, 15953.
8. (a) J. S. Park, Y. J. Yoo, J.S. Hwang, J. H. Kang, B. W. Lee, Y. P. Lee, *J. Appl. Phys.,* 2014, **115**, 013904. (b) M. S. Mandar, C. Hao, X. Dong, T. Guo, L. Zhang, M. Li, H. Wang, *Nanoscale***,** 2014, **6**, 4735.
9. A. Reyes, C. de la Vega, E. Fuentes Ma, L. Fuentes, *J. Eur. Ceram. Soc.,* 2007, **27**, 3709.
10. G. Catalan, J. F. Scott, *Adv. Mater.,* 2009, **21**, 2463.
11. I. Sosnowska, T. P. Neumaier, E. Streichele, *J. Phys. C,* 1982, **15**, 4835.
12. Y. F. Popov, A. K. Zvezdin, G. P. Vorobev, A. M. Kadomtseva, V. A. Murashev, D. N. Rakov, *JETP Lett*., 1993, **57**, 69.
13. (a) W. Ramadan, A. P. Shaikh, S. Ebrahim, A. Ramadan, B. Hannoyer, S. Jouen, X. Sauvage, S. Ogale, *J. Nanopart. Res.,* 2013, **15**, 1848. (b) S. Y. Yang, L. W. Martin, S. J. Byrnes, T. E. Conry, S. R. Basu, D. Paran, L. Reichertz, J. Ihlefeld, C. Adamo, A. Melville, Y. H. Chu, et. al., *Appl. Phys. Lett.,* 2009, **95**, 062909.
14. (a) J. Deng, S. Banerjee, K. S. Mohapatra, R. Y. Smith, M. Misra, *Journal of Fundamentals of Renewable Energy and Applications,* 2011, **1**, Article ID R101204, 10 pages, doi:10.4303/jfrea/R101204. (b) L. Fei, J. Yuan, Y. Hu, C. Wu, J. Wang, Y. Wang, *Cryst. Growth Des.,* 2011, **11**, 1049. (c) S. Li, Y. H. Lin, B. P. Zhang, Y. Wang, C. W. Nan, *J. Phys. Chem. C*, 2010, **114**, 2903. (d) F. Gao, X. Y. Chen, K. B. Yin, S. Dong, Z. F. Ren, F. Yuan, T. Yu, Z. G. Zou, J. M. Liu, *Adv. Mater.,* 2007, **19**, 2889.
15. (a) L. Li, P. A. Salvador, G. S. Rohrer, *Nanoscale*, 2014, **6**, 24. (b) L. Li, X. Liu, Y. Zhang, N. T. Nuhfer, K. Barmak, P. A. Salvador, G. S. Rohrer, *ACS Appl. Mater. Interfaces*, 2013, **5**, 5064.
16. (a) Y. Cui, J. Briscoe, S. Dunn, *Chem. Mater.,* 2013, **25**, 4215. (b) M. Stock, S. Dunn, *J. Phys. Chem. C,* 2012, **116**, 20854.
17. (a) A. Zhu, Q. Zhao, X. Li, Y. Shi, *ACS Appl. Mater. Interfaces,* 2014, **6**, 671. (b) Z. Li, Y. Shen, Y. Guan, Y. Hu, Y. Lin, C. W. Nan, *J. Mater. Chem. A,* 2014, **2**, 1967. (c) Z. Li, Y. Shen, C. Yang, Y. Lei, Y. Guan, Y. Lin, D. Liu, C. W. Na, *J. Mater. Chem. A,* 2013, **1**, 823.
18. (a) R. Guo, L. Fang, W. Dong, F. Zheng, M. Shen, *J. Phys. Chem. C*, 2010, **114**, 21390. (b) C. Madhu, B. M. Bellakki, V. Manivanan, *Indian Journal of Engineering & Materials,* 2010, **17**, 131. (c) M. Sakar, S. Balakumar and S. Ganesamoorthy, *J. Mater. Chem. C,* 2014, **2**, 6835-6842.
19. (a) G. Cernuto, N. Masciocchi, A. Cervellino, G. M. Colonna, A. Guagliardi, *J. Am. Chem. Soc.,* 2011, **133**, 3114. (b) H. Xu, W. Wang, W. Zhu, *J. Phys. Chem. B*, 2006, **110**, 13829.
20. B. Weng, S. Liu, Z. R. Tang, Y. J. Xu, *RSC Adv.,* 2014, **4**, 12685.
21. Z. Zhen, W. Ping, C. Lang, W. Junling, *Appl. Phys. Lett.,* 2010, **96**, 012905.
22. M. Sakar, S. Balakumar, I. Bhaumik, P. K. Gupta, S. N. Jaisankar, *RSC Adv.,* 2014, **4**, 16871.
23. (a) M. Sakar, S. Balakumar, P. Saravanan and S. Bharathkumar, *Nanoscale*, 2015, **7**, 10667. (b) M. Sakar, S. Balakumar, *RSC Adv.,* 2013, **3**, 23737.
24. S. R. Shannigrahi, A. Huang, N. Chandrasekhar, D. Tripathy, A. O. Adeyeye, *Appl. Phys. Lett.,* 2007, **90**, 022901.
25. (a) P. D. Dutta, P. B. Mandal, R. Naik, G. Lawes, A. K. Tyagi, *J. Phys. Chem. C,* 2013, **117**, 2382. (b) P. D. Dutta, P. B. Mandal, M. D. Mukadam, S. M. Yusuf, A. K. Tyagi, *Dalton Trans.*, 2014, **43**, 7838.
26. B. S. Zhang, Z. C. Quan, T. J. Zhang, T. Guo, S. B. Mo, *J. Appl. Phys.,* 2007, **101**, 014107.
27. J. F. Moulder, W. F. Stickle, P. E. Sobol, K. D. Bomben, Handbook of X-ray photoelectron spectroscopy, Perkin-Elmer Corporation, Minnesota, 1992.
28. Z. Quan, H. Hu, S. Xu, W. Liu, G. Fang, M. Li, X. Zhao, *J. Sol-Gel Sci. Technol.,* 2008, **48**, 261.
29. Y. Wang, Q. H. Jiang, H. C. He, C. W. Nan, *Appl. Phys. Lett.*, 2006, **88**, 142503.
30. (a) Z. Lu, H. Che, R. Robert, Y. X. B. Zhu, J. Deng, L. Wu, C. Y. Chung, P. C. Grey, *Chem. Mater.,* 2011, **23**, 2848. (b) K. Y. Chew, M. A. Bakar, N. H. H. A. Bakar, *Modelling and Numerical Simulation of Material Science,* 2013, **3**, 23.
31. J. Wang, G. Zhu, L. Deng, L. Kang, Z. Hao, Z. Liu, *CrystEngComm,* 2012, **14**, 8253.
32. S. D. Kilin, V. O. Prezhdo, Y. Xia, *Chem. Phys. Lett.,* 2008, **458**, 113.
33. Y. Xiong, *Chem. Commun.,* 2011, **47**, 1580.
34. S. Sasaki, N. Kubota, N. Doki, *Chem. Eng. Technol.,* 2006, **29**, 247.
35. A. B. Murphy, *Solar Energy Materials & Solar Cells,* 2007, **91**, 1326.
36. F. Huang, Z. Wang, X. Lu, J. Zhang, K. Min, W. Lin, R. Ti, TingTing Xu, Ju He, Chen Yue, Jinsong Zhu, *Sci. Rep.,* 2013, **3**, 2907.
37. S. S. Pillai, G. Rangarajan, N. P. Raju, A. J. Epstein, P. N. Santhosh, *J. Phys.: Condens. Matter,* 2007, **19**, 496221.
38. C. Binns, M. J. Maher, Q. A. Pankhurst, D. Kechrakos, K. N. Trohidou, *Phys. Rev. B,* 2002, **66**, 184413.
39. H. Mamiya, I. Nakatani, T. Furubayashi, *Phys. Rev. Lett.,* 1998, **80**, 177.
40. M. K. Singh, W. Prellier, M. P. Singh, R. S. Katiyar, J. F. Scott, *Phys. Rev. B,* 2008, **77**, 144403.
41. J. A. Rondinone, C. S. A. Samia, Z. J. Zhang, *J. Phys. Chem. B,* 1999, **103**, 6876.
42. L. Neel, In Low Temperature Physics; Dewitt, C., Dreyfus, B., de Gennes, P. D., Eds.; Gordon and Beach: New York, 1962; p 413.
43. (a) D. P. Dutta, G. Sharma, A. K. Rajarajan, S. M. Yusuf, G. K. Dey, *Chem. Mater.,* 2007, **19**, 1221. (b) J. C. Denardin, A. L. Brandl, M. Knobel, P. Panissod, A. B. Pakhomov, H. Liu, X. X. Zhang, *Phys. Rev. B,* 2002, **65**, 064422.
44. M. Sakar, S. Balakumar, P. Saravanan, S. N. Jaisankar, *Mat. Res. Bul.,* 2013, **48**, 2878.
45. (a) S. T. Zhang, M. H. Lu, D. Wu, Y. F. Chen, N. B. Ming, *Appl. Phys. Lett.* 2005, **87**, 262907, (b) S. R. Shannigrahi, A. Huang, D. Tripathy, A.O. Adeyeye, *J. Magn. Magn. Mater.,* 2008, **320**, 2215. (c) M. Y. Sun, P. Li, C. Jin, L. Y. Wang, D. X. Zheng, H. L. Bai, *EPL,* 2014, **105**, 17007.
46. (a) W. H. Meiklejohn, C. P. Bean, *Phys. Rev.,* 1956, **102**, 1413. (b) J. Nogues, I. K. Schuller, *J. Magn. Magn. Mater.,* 1999, **192**, 203.

47. (a) A. Berkowitz, K. Takano, *J. Magn. Magn. Mater*., 1999, **200**, 552. (b) R. L. Stamps, *J. Phys. D,* 2000, **33**, R247. (c) M. Kiwi, *J. Magn. Magn. Mater*., 2001, **234**, 584.
48. (a) Y. Ijiri, T. C. Schulthess, J. A. Borchers, P. J. van der Zaag, R. W. Erwin, *Phys. Rev. Lett*., 2007, **99**, 147201. (b) S. Dong, K. Yamauchi, S. Yunoki, R. Yu, S. Liang, A. Moreo, J. M. Liu, S. Picozzi, E. Dagotto, *Phys. Rev. Lett.,* 2009, **103**, 127201.
49. R. Yanes, J. Jackson, L. Udvardi, L. Szunyogh, U. Nowak, *PRL,* 2013, **111**, 217202.
50. D. L. Fox, J. F. Scott, *J. Phys. C: Solid State Phys*., 1977, **10**, L329.
51. C. Ederer, J. Craig Fennie, *J. Phys.: Condens. Matter,* 2008, **20**, 434219.
52. (a) Q. Zhang, W. Gong, J. Wang, X. Ning, Z. Wang, X. Zhao, W. Ren, Z. Zhang, *J. Phys. Chem. C,* 2011, **115**, 25241. (b) T. J. Park, C. G. Papaefthymiou, R. A. Moodenbaugh, Y. Mao, S. S. Wong, *J. Mater. Chem.,* 2005, **15**, 2099.
53. (a) X. Zhang, V. Thavasi, S. G. Mhaisalkar, S. Ramakrishna, *Nanoscale*, 2012, **4**, 1707. (b) N. K. Elumalai, R. Jose, P. S. Archana, V. Chellappan, S. Ramakrishna, *J. Phys. Chem. C*, 2012, **116**, 22112.
54. (a) A. Leelavathi, G. Madras, N. Ravishankar, *Phys. Chem. Chem. Phys.,* 2013, **15**, 10795. (b) H. J. Yun, H. Lee, J. B. Joo, W. Kim, J. Yi, *J. Phys. Chem. C,* 2009, **113**, 3050.
55. (a) H. Huang, E. D. Gross, X. Yang, S. J. Moore, L. Zang, *ACS Appl. Mater. Interfaces,* 2013, **5**, 7704. (b) M. Supur, Y. Yamada, E. M. El-Khouly, T. Honda, S. Fukuzumi, *J. Phys. Chem. C,* 2011, **115**, 15040.
56. (a) A. N. Benedek, J. C. Fennie, *J. Phys. Chem. C,* 2013, **117**, 13339. (b) C. R. Bowen, H. A. Kim, P. M. Weaver, S. Dunn, *Energy Environ. Sci.,* 2014, **7**, 25. (c) S. Park, C. W. Lee, M. G. Kang, S. Kim, H. J. Kim, J. E. Kwon, S. Y. Park, J. Y. Kang, K. S. Hong, K. T. Nam, *Phys. Chem. Chem. Phys.,* 2014, DOI: 10.1039/C4CP01267D
57. (a) P. M. Rorvik, T. Grande, M. A. Einarsrud, *Adv. Mater.*, 2011, **23**, 4007. (b) S. Dunn, M. Stock, MRS Proceedings, 2012, **1446**, DOI: http://dx.doi.org/10.1557/opl.2012.870.
58. Y. S. Park, J. H. Kim, W. Yang, *Surf. Interface Anal.,* 2012, **44**, 759.
59. M. M. Haque, D. Bahnemann, M. Muneer, Photocatalytic Degradation of Organic Pollutants: Mechanisms and Kinetics, Organic Pollutants Ten Years After the Stockholm Convention - Environmental and Analytical Update, Dr. Tomasz Puzyn (Ed.), ISBN: 978-953-307-917-2, InTech, 2012, DOI: 10.5772/34522.
60. Q. J. Ruan, W. D. Zhang, *J. Phys. Chem. C,* 2009, **113**, 4168.
61. R. S. Knox, Theory of Excitons, Solid State Physics, Suppl. 5, edited by F. Seitz, D. Turnbull, Academic Press, 1963.
62. A. Tsukernik, D. Cheskis, O. Potashnik, A. Palevski, S. Bar-Ad, S. Luryi, A. Cho, *Eur. Phys. J. B,* 2001, **23**, 341.

